Icarus 226 (2013) 1559–1567

Contents lists available at ScienceDirect

Icarus

journal homepage: www.elsevier.com/locate/icarus

Hubble observations of Jupiter's north–south conjugate ultraviolet aurora

J.-C. Gérard [a,*], D. Grodent [a], A. Radioti [a], B. Bonfond [a], J.T. Clarke [b]

[a] LPAP, Université de Liège-B5c, 17 allée du 6 août, 4000 Liège, Belgium
[b] Center for Space Physics, Boston University, Commonwealth Avenue, 725 Boston, MA 02215, USA

ARTICLE INFO

Article history:
Received 31 March 2013
Revised 24 July 2013
Accepted 14 August 2013
Available online 30 August 2013

Keywords:
Aurora
Jupiter
Ultraviolet observations
Magnetospheres

ABSTRACT

Comparisons of the northern and southern far ultraviolet (UV) auroral emissions of Jupiter from the Hubble Space Telescope (HST) or any other ultraviolet imager have mostly been made so far on a statistical basis or were not obtained with high sensitivity and resolution. Such observations are important to discriminate between different mechanisms responsible for the electron acceleration of the different components of the aurora such as the satellite footprints, the «main oval» or the polar emissions. The field of view of the ACS and STIS cameras on board HST is not wide enough to provide images of the full jovian disk. We thus compare the morphology of the north and south aurora observed 55 min apart and we point out similarities and differences. On one occasion HST pointed successively the two polar regions and auroral images were seen separated by only 3 min. This makes it possible to compare the emission structure and the emitted FUV power of corresponding regions. We find that most morphological features identified in one hemisphere have a conjugate counterpart in the other hemisphere. However, the power associated with conjugate regions of the main oval, diffuse or discrete equatoward emission observed quasi-simultaneously may be different in the two hemispheres. It is not directly nor inversely proportional to the strength of the *B*-field as one might expect for diffuse precipitation or field-aligned acceleration with equal ionospheric electron density in both hemispheres. Finally, the lack of symmetry of some polar emissions suggests that some of them could be located on open magnetic field lines.

1. Introduction

The morphology of Jupiter's ultraviolet aurora has been investigated with the Hubble Space Telescope in some detail over the last 20 years. In a first approximation, four distinct regions of emissions may be distinguished (Clarke et al., 2004). First, a main oval or more correctly main emission is clearly identified on the morning side and sometimes in the afternoon. Second, occasionally rapidly varying bright regions are observed poleward of the main emission. Third, the outer emissions, formed by either diffuse, patchy or arc-shaped emissions located equatorward of the main oval. Finally, the satellite footprints, located near the feet of the field lines connected to the moons Io, Europa and Ganymede (Bonfond et al., 2012). Important statistical differences between the morphology of the main emission in the north and in the south have been pointed out since the two polar regions have been observed. They reflect the large asymmetry of the surface magnetic field which is strongly non-dipolar and presents a magnetic anomaly in the north (Grodent et al., 2008; Hess et al., 2011). Accumulation of observations in both hemispheres at different central meridian longitudes has made it possible to obtain statistical maps of the morphology of the main emissions and satellite footprints (Clarke et al., 2002; Grodent et al., 2003a, 2008). Major differences reflecting the characteristics of the surface jovian magnetic field appear when comparing these composite polar maps. While the south auroral region is relatively circular around the magnetic pole, the north main emission exhibits a kidney shape extending down to 55° in the 170° System III longitude (λ_{III}) sector but only to 85° near λ_{III} = 50°. A consequence of this longitudinal asymmetry is that, from Earth orbit, the visibility of the aurora strongly depends on the value of the central meridian longitude (CML). The best view of the north aurora is obtained for λ_{III} close to 170°, while the south offers optimum visibility near 50°, a longitude where the north aurora is hardly visible. This asymmetry has driven observational biases and limitations. One is that the majority of the available HST auroral images were collected in the north. Another one is the difficulty to obtain simultaneous good views of both polar regions. This latter point, coupled with the limited field of view of the FUV imaging instruments on board Hubble has severely restricted studies of conjugate jovian aurora. The Wide Field and Planetary Camera II (WFPC2) was able to image the full planet but its sensitivity was more than an order of magnitude less than later equipment and comparisons of the two hemispheres were

* Corresponding author.
E-mail address: jc.gerard@ulg.ac.be (J.-C. Gérard).

0019-1035/$ - see front matter © 2013 Elsevier Inc. All rights reserved.
http://dx.doi.org/10.1016/j.icarus.2013.08.017

therefore limited. Within these limitations, a great deal of magnetic conjugacy was observed between the north and south aurora (Clarke et al., 1996; Ballester et al., 1996). More recent sensitive cameras on board Hubble such as the Space Telescope Imaging Spectrograph (STIS) or the Advanced Camera for Surveys (ACS) cannot provide visibility of the full planet. Consequently, only one hemisphere has been observed at a time and a period extending from hours to days generally separated consecutive images of the north and south aurora. Occasionally, the telescope pointed on one hemisphere during one HST orbit and the opposite one during the next orbit. For example, Radioti et al. (2009b) presented polar projections of the two hemispheres showing features such as the main oval, the Io footprint and the equatorial diffuse emission in both hemispheres. So far, only statistical studies (Grodent et al., 2003a) have systematically compared the morphological characteristics of the north and south aurora. The difficulty to account for the different viewing geometry of the two hemispheres has also prevented comparison of the auroral power emitted in the north and the south. Globally, it is not therefore known whether the total power of the main auroral emission is stronger in one hemisphere.

At Earth, conjugate observations of the polar aurora have shown that, in a first approximation, the aurora borealis and aurora australis are mirror images of each other since particles causing the emission follow the magnetic field lines connecting the two hemispheres. However, concurrent observations have indicated that corresponding auroral features may be displaced by several tens of degrees of longitude (Østgaard et al., 2007) and seasonal effects can generate hemispherical differences in brightness (Newell et al., 1996). Additionally, bright spots have been simultaneously observed at dawn in the northern summer hemisphere and at dusk in the southern winter hemisphere (Laundal and Østgaard, 2009). Several processes have been proposed to explain these hemispheric asymmetries. One is the difference of the magnetic field strength at conjugate points that may generate differences in the precipitated energy flux (Stenbaek-Nielsen et al., 1973). Second, a different electrical conductivity between the summer and winter polar regions is a source of asymmetry in the electric field accelerating auroral electrons if the magnetosphere acts as a current generator. Seasonal effects can also create inter-hemispheric field aligned currents (Benkevich et al., 2000) that are the sources of asymmetrical auroral features. Third, the orientation of the interplanetary magnetic field and the value of the B_y component in particular (Fillingim et al., 2005) plays an important role on auroral asymmetries (Østgaard et al., 2005).

The smaller angular size of Saturn than Jupiter makes it possible to collect images of the full planet with the ACS and the STIS cameras. Such data were obtained at equinox by Nichols et al. (2009). They showed that individual auroral features can exhibit distinct hemispheric asymmetries. They listed possible causes of these asymmetries such as the short observation timescale relative to the auroral Alfvén wave propagation time, the asymmetric SKR phases, or small scale variations of the Pedersen conductivity. They also found that the radius of the northern auroral oval is ~17% smaller than the southern but the total emitted UV power is on average ~17% larger in the north than the south. They suggested that the polar magnetic field is larger in the north than in the south in the same proportion and that field-aligned currents (FACs) are responsible for the emission. Based on the same dataset, Meredith et al. (2013) showed that Eastward-propagating patches frequently observed in the dawn-to-noon sector were generally not closely conjugate, but typically displaced in local time by ~0.5–1 h. They indicated that asymmetric polar auroras are expected on Saturn on the basis of reconnection with an IMF dominated by B_y. They suggested that modes of ULF field line resonances produce hemispherically anti-symmetric field-aligned currents, leading to auroral emission in one hemisphere with no conjugate counterpart.

No similar study has been carried out in the case of the jovian aurora, essentially because of the lack of parallel observations of the two auroral regions with sufficient spatial resolution and sensitivity. However, noticeable statistical asymmetries in the structure of Io's magnetic footprint have been initially described by Gérard et al. (2006) who found that, at a given time, the multiplicity and inter-distance of the multiple footprint spots may be widely different in the two hemispheres. Bonfond et al. (in press) observed obvious north/south statistical asymmetries in the footprint brightness. Hess et al. (in press) attributed these differences to asymmetries of the magnetic field leading to variations in every step in the long chain of processes leading to the precipitation of the electrons.

In this study, we take advantage of several observations of the two jovian hemispheres specifically planned during the 2007 HST campaign of observations of the jovian aurora. Some of them were separated in time by two consecutive HST orbits, but on one occasion high spatial resolution images offering quasi-simultaneous images with an acceptable view of both hemispheres were acquired with Hubble. We first compare the morphological features of two couples of images separated by one HST orbit. We then concentrate on the quasi-simultaneous case and describe the results of a quantitative comparison of the brightness of magnetically conjugate auroral features. We finally discuss the implications of the N/S brightness asymmetries on the processes involved in the auroral electron energization.

2. Observations

The observations described in this study were collected during the HST campaign of jovian and kronian auroral imaging whose main objective was to investigate the response to solar wind variations of auroral morphology and brightness. The full list of observations during the campaign and their time distribution were given by Clarke et al. (2009). The Jupiter images were collected between February 10 and June 11, 2007. FUV exposures of Jupiter and Saturn were obtained using the Solar Blind Channel (SBC) of the HST Advanced Camera for Surveys (ACS) (Gonzaga et al., 2013). In addition to quasi-daily observations of the jovian north or south regions, a few HST visits were specifically designed to study the auroral conjugacy analyzed in this work. During these periods, one hemisphere was imaged with ACS, followed 55 min later by an observation of the other hemisphere during the next HST orbit. Each ACS exposure lasted 100 s, a compromise between suitable S/N ratio and the blurring effect of the planetary rotation. Two such couples of north–south images will be discussed here. In addition, on twelve occasions, the Space Telescope was slewed from one polar region to the other during the same HST orbit. All but one of them were obtained for values of the central meridian longitude providing suitable observing conditions of the main emission for only one hemisphere. Table 1 lists the dates, start times and sequences of the three sets of conjugate observations discussed in this study. These images were collected with the F125LP filter

Table 1
List of ACS exposures from the 2007 HST campaign described in this study.

Date	Time	Hemisphere	CML (λ_{III})	Figure (panels)
June 11	04:35	S	99°	1(2), 1(4)
June 11	05:00	N	133°	1(1), 1(3)
February 27	09:35	S	114°	2(2), 2(4)
February 27	10:29	N	147°	2(1), 2(3)
March 22	23:04	N	105°	3(1), 4(1)
March 22	23:07	S	107°	3(2), 4(2)
March 22	23:19	S	115°	3(3), 4(3)
March 22	23:22	N	116°	3(4), 4(4)

which rejects most of the Ly-α geocoronal and planetary contributions. However, the ACS/SBC camera is affected by "red leak" from longer wavelengths, mostly caused by the reflected solar light. We applied dark count subtraction, flat-fielding as well as geometrical corrections to the images considered in this study. The reflected solar light contribution from the disk of the planet was modeled and we subtracted an empirically built planetary disk contribution following the method described by Bonfond et al. (2011). For higher accuracy, we additionally subtracted the mean residual brightness measured in two 20-pixel wide squares located 5° north and south of the emission region considered. The conversion rates from count rate on the detector to brightness and emitted power have been computed by Gustin et al. (2012).

The transmission of the F125LP filter used for these observations sharply drops longward of Ly-α, thus avoiding contamination from geocoronal emissions. It peaks near 132 nm and slowly drops at longer wavelengths. The values given in this study are the power (in Watts) emitted by H_2 molecules in the 70–180 nm wavelength range. The Point Spread Function (PSF) of the ACS camera depends on the filter used for the observations. It was determined using an algorithm based on the non-violation of the sampling theorem (Magain et al., 2007). The Full Width at Half Maximum (FWHM) of the PSF lies between 2 and 3 pixels. Most of the following discussion is based on polar (orthographic) projections of the auroral features. The pointing accuracy of the guide star acquisition mode used for these observations is not sufficient for that purpose. As a consequence, Jupiter's center position is determined using the limb fitting method described in details by Bonfond et al. (2009).

3. Results

The analysis of the conjugate morphology proceeds in two steps. We first compare the morphology and the magnetically conjugate auroral structures observed in the two hemispheres. In a second step, we determine the emitted power of conjugate structures and compare the power ratio of the two regions with the intensity of the local surface magnetic field.

3.1. Morphological features

As mentioned before, we first concentrate on ACS images collected on two consecutive HST orbits on June 11, 2007 (case 1). The first two panels of Fig. 1 show the north (1) and south (2) polar aurora. The north image was collected about 56 min after the south one. The central meridian longitudes (1: 133°, 2: 99°) of the planet during the exposures were well suited to obtain optimal view of the two auroral regions. During the 56 min separating the two images, the planet rotated by ~35°. The following two panels show the polar projections in the north (3) and south (4) in System III coordinates with the 180° meridian oriented to the bottom. In panel (4), the south polar projection is displayed as if the aurora was seen from above the north pole through the planet. The anticlockwise displacement of the global morphology is a consequence of the distortion of the jovian magnetic field lines that are twisted eastward between their north and south footprints in this longitude sector. For example, the Ganymede footprint mapping to an equatorial radial distance of $15R_J$, close to the source region of the main oval, is observed in the south to be shifted by ~60° from its north counterpart at Ganymede's longitude λ_{III} = 140° (Grodent et al., 2009). For comparison, the statistical (Grodent et al., 2003a) locations of the main auroral oval and the locus of Io footprint and tail ($6R_J$ mapping) are indicated by the dashed green lines. As can be readily observed, in this case both the main auroral emission and the Io footprint closely coincide with their statistical location at most longitudes in both hemispheres. The enhanced brightness observed near the edges of the main emission on both sides of the images stems from the proximity to the planetary limb. We note that auroral features such as the polar emissions frequently observed inside the main emission region exhibit rapid variations with characteristic times on the order of 100 s (Waite et al., 2001; Grodent et al., 2003b; Gérard et al., 2003; Bonfond et al., 2011). Given the longer time separating images of the two hemispheres, these features will not be discussed in detail in this study. Instead, the main emission structure is generally stable over several hours (Nichols et al., 2009) as evidenced by observations of the morphology during one or several successive HST orbits (movie available as supporting material in Nichols et al. (2009); jgra19860-sup-0003-ms01.mp4).

A series of similarities are easily identifiable when comparing the polar projections. First, a secondary arc parallel to and located equatorward of the main emission is observed at λ_{III} values less than 167° in both hemispheres. The behavior of such partial secondary oval was described by Grodent et al. (2003a) who noted that it is generally present at $100° < \lambda_{III} < 180°$ when the CML ranges between 110° and 220°. They speculated this auroral emission may be associated with a first region of FACs transmitting the torque from the ionosphere to the magnetosphere to enforce plasma corotation. Second the red rectangles indicate an auroral feature located equatorward of the main emission, which is probably related to magnetospheric plasma injections. Similar auroral structures have been reported by Mauk et al. (2002) and were interpreted as auroral signatures of plasma injections at Jupiter. Third, the Io footprint is about significantly brighter in the south than is the north.

We now examine the longitudinal extent of the dimmer "discontinuity" region indicated by the yellow lines on the two polar projections. It is regularly observed as a region, fixed in local time, where the brightness of the main emission significantly drops below the level of the adjacent segments of the main oval. Radioti et al. (2008) defined it as the main emission region with a brightness less than 10% of the brightest region of the oval. Panels (5) and (6) of Fig. 1 represent the smoothed intensity measured in the unprojected images along the main emission. Vertical bars A and B and C and D represent our best estimate of the limits of the discontinuity in the north and south respectively. We note that a region of enhanced emission is seen near the middle of the AB segment. It corresponds to a brightening which was probably not present at the time of the south exposure, about 56 min earlier. Therefore, the criterion used by Radioti et al. (2008) has not been applied in this case. In the present observations, the discontinuity extends over 11,450 km in the north (AB) and 20,700 km in the south (CD). If we magnetically map the size of the north discontinuity to the south using the VIPAL model (Hess et al., 2011), we find that it would extend over ~15,000 km, that is less than the observed length. The presence of these segments of the main oval showing no or weak emission in a confined magnetic local time sector was studied by Radioti et al. (2008). They explained its presence in terms of reduced or downward field aligned currents flowing to the middle magnetosphere in the pre-noon and early afternoon sector. They showed that it corresponds to regions where Pioneer, Voyager and Galileo observed a reduced or downward field-aligned current, in agreement with model predictions and in situ measurements of ion flow speeds in the equatorial plane. This asymmetry will be further discussed following description of another couple of conjugate images.

We now examine the second set of N/S images collected on February 27, 2007 (case 2). Fig. 2 shows the raw images (panels 1 and 2) and the projections in polar coordinates (3 and 4) similar to Fig. 1. As for case 1, a number of similarities are observed such as the presence of a secondary oval quasi-parallel to the main oval equatorward of the main emission, although in different longitudi-

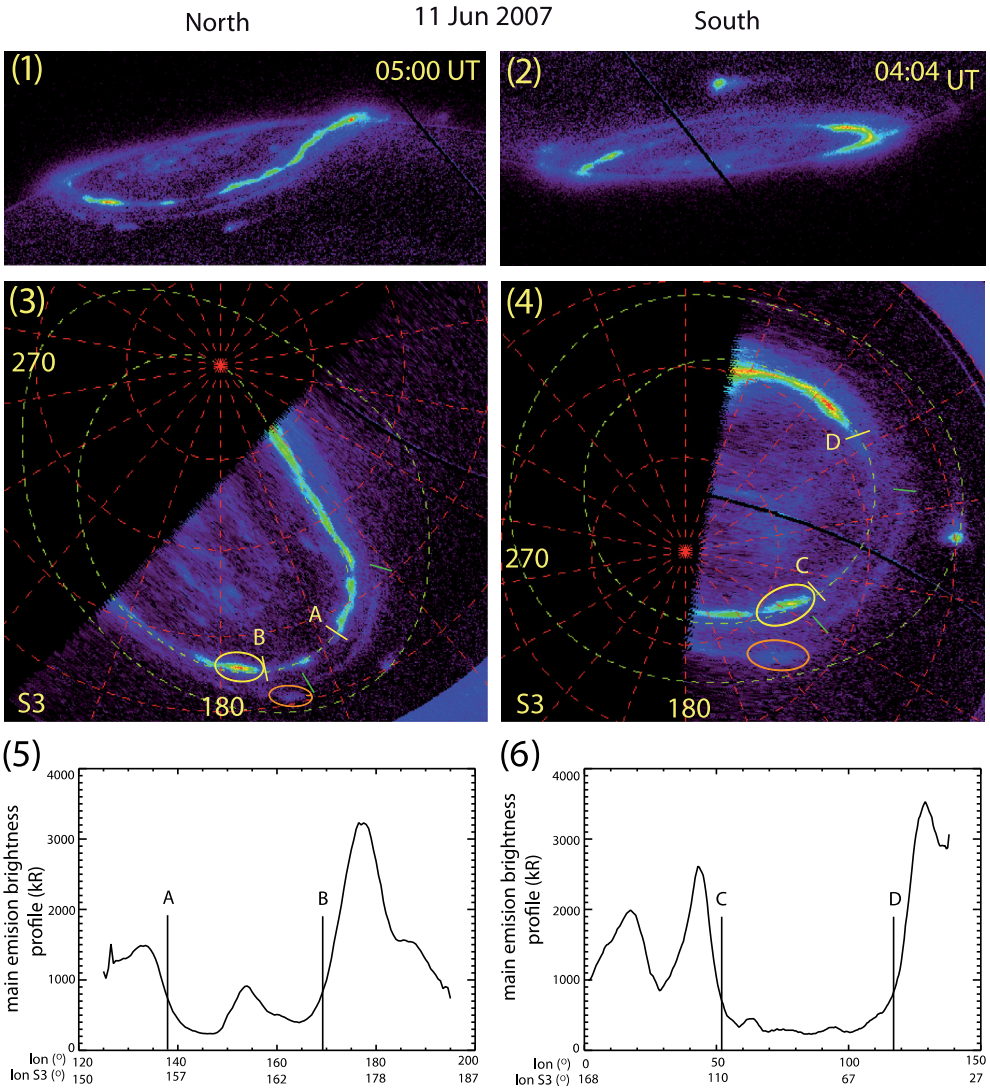

Fig. 1. Raw images of the aurora obtained with the ACS camera on June 11, 2007 in the north (panel 1) and south (panel 2). The dark line feature crossing images 2 and 4 is caused by is caused by a bad anode in the ACS/SBC MAMA detector. Projections are shown in (3) and (4) in polar coordinates with the System III 180° meridian oriented toward the bottom of the page. The two images are separated by 56 min. The yellow bars indicate the limits of the discontinuity in the main emission. The ellipses define the regions where the emitted power is determined in the main (yellow) and outer emission regions (red) and the vertical green line the secondary oval the power of which is estimated (Table 2). The color scale is identical for the north and south images. Panels (5) and (6) show the brightness along the main oval with vertical bars indicating the limits of the auroral discontinuity region.

nal sectors. A broad region of diffuse aurora extends from the dusk limb to about 160°, equatorward of the main oval in both hemispheres. This type of unstructured diffuse emission was discussed by Radioti et al. (2009b) and interpreted as the signature of electrons scattering into the loss cone by whistler mode waves leading to precipitation into the atmosphere. We also note that the main emission in the north lies slightly poleward of the statistical oval, unlike the south emission which is located significantly poleward of the south oval at all longitudes, except near the morning limb, the region where polar projections are less reliable. The brightness distribution along the main emission in the discontinuity region is shown in panels (5) and (6). As in case 1, we have used our best estimate of the discontinuity limits, considering the complex structure of the intensity distribution in the southern aurora. The extension is 13,200 km in the north (AB) and 33,900 km in the south (CD). We estimate the size of the north discontinuity mapped in the south, based on the VIPAL model as in case 1 and we expect it to be ~15,100 km, considerably less than the observed value. Such a large difference is unexpected considering that the source region of the discontinuity was shown to be fixed in local time. In both cases 1 and 2, our evaluation of the extent of the south discontinuity is smaller than expected on the basis of the magnetic mapping from the north to the south. The difference is particularly pronounced in the images obtained on February 27.

We finally compare the morphology of the March 22, 2007 observations (case 3). Fig. 3 illustrates the timing of the observation sequence as the telescope field of view slewed from the north to the south and back to north during a single HST orbit. The last exposure of the first north visit (image 1) started at 23:04 UT, the field of view was moved to the south and started observing at 23:07 (image 2), leaving a gap of about 3 min. The last south image started at 23:19 (image 3), before the telescope slewed back to the north polar aurora and obtained a north image at 23:22 (image 4). Consequently, the time separating the two sets of N–S comparisons does not exceed 3 min, a short time compared to the temporal variations observed outside the polar regions. The CML increased by 11.1° between images 1 and 4, but it changed by only

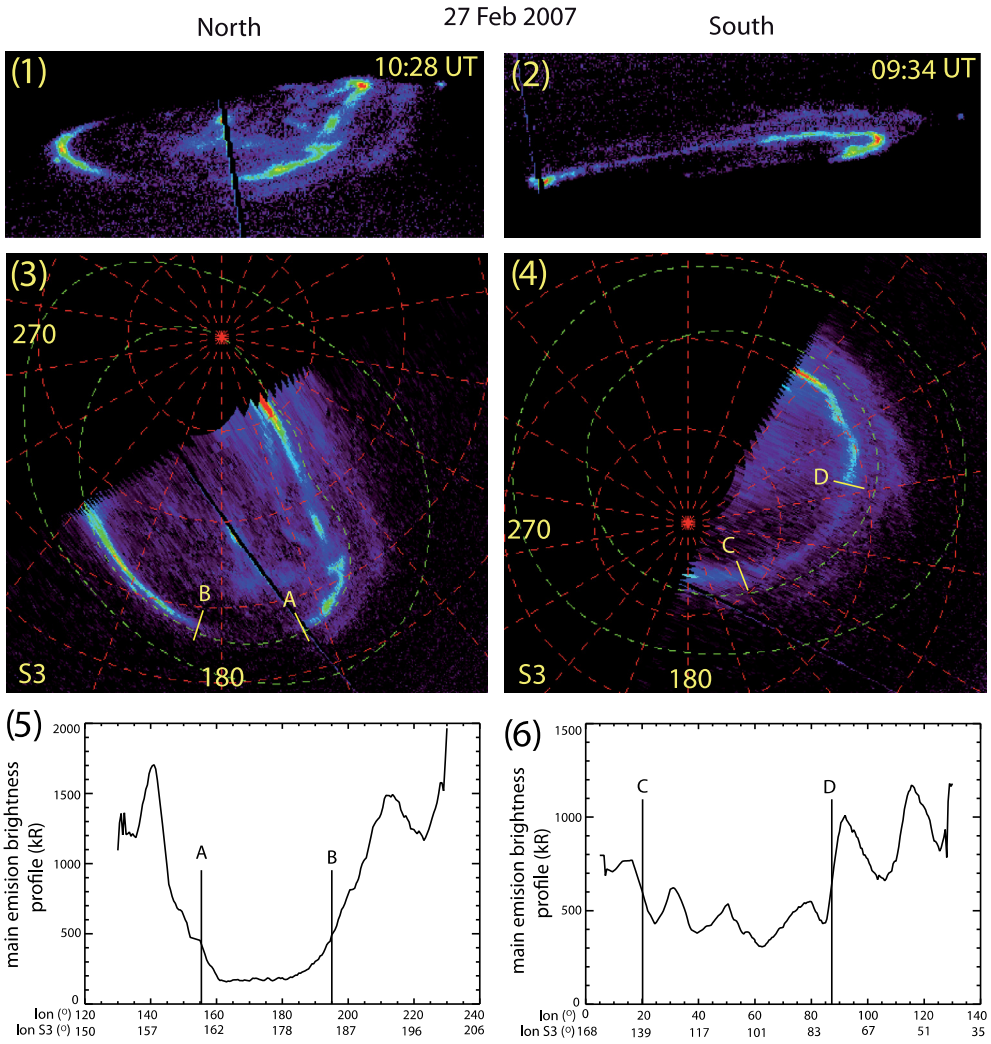

Fig. 2. Raw images of the aurora obtained with the ACS camera on February 27, 2007 in the north (1) and south (2). The dark line feature crossing images 2 and 4 is caused by is caused by a bad anode in the ACS/SBC MAMA detector. Projections are shown in (3) and (4) in polar coordinates with the System III 180° meridian oriented toward the bottom of the page. The two images are separated by 54 min. The yellow bars indicate the limits of the discontinuity in the main emission. The color scale is identical for the north and south images. The dark feature crossing the images is caused by a bad anode in the ACS/SBC MAMA detector. The two images are separated by 54 min. Panels (5) and (6) show the brightness along the main oval with vertical bars indicating the limits of the auroral discontinuity region.

2° between the north and the south exposures used for this comparison.

The polar projections of the four images are shown in Fig. 4. We first note an important difference between the two images: some

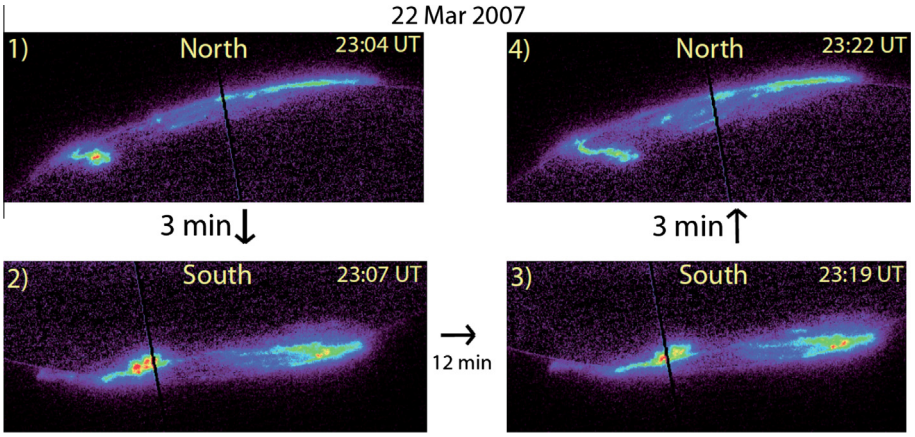

Fig. 3. Sequence of four images obtained with the ACS camera on March 22, 2007 during the same HST orbit: in the north (1), south (2, 3) and back in the north (4) polar regions.

bright polar emissions are present in the northern hemisphere with no counterpart in the south. Although it is known that the polar aurora is generally time variable, in this case the asymmetry in the polar auroras is maintained throughout the intervening images, and is therefore real and significant. The lack of symmetry in the behavior of polar emissions suggests that they are located on magnetic field lines which are not common. We interpret this asymmetry as a possible indication they these field lines are open. Meredith et al. (2013) showed that asymmetric auroras on Saturn are expected on the basis of reconnection with an interplanetary magnetic field dominated by its B_y component.

The main oval is essentially absent in sectors between the dusk limb and 140° in image 1, where only polar diffuse emission is observed. By contrast, it is clearly observed in image 1 of Fig. 3 and image 1 of Fig. 4 at CMLs larger than 140°. The same applies to image 3 whose polar projection shows very little change compared to image 1 taken 18 min earlier. We note little change between images 2 and 3, confirming the stability of the morphology and intensity of the precipitation during the 12 min of observations of the south aurora. The main emission is located poleward of the statistical oval at all longitudes in both hemispheres. At around 170°N and 130°S, close to the main emission, a particular structure is observed, marked by the orange rectangles on the projection. This structure deviates from the main emission and is therefore considered as a separate feature, which might be related to plasma injections in the magnetosphere, as discussed in Fig. 1. The size of the structure in the south is much larger than the one in the north similar to the equivalent feature in Fig. 1. This size difference possibly reflects the difference in the magnetic field in the two hemispheres and the convergence of the magnetic field line. In the following, we proceed with a quantitative comparison of the auroral power of different auroral features.

3.2. Intensity of conjugate regions

The intensity of auroral features is frequently expressed in surface brightness units such as kiloRayleighs (kR) (1 kR is equal to $4\pi B$, where B is the apparent surface brightness expressed in 10^9 - photons/cm^2 s ster). A drawback is that the intensity expressed in kR depends on the orientation of the observer and is generally converted into a virtual "vertical intensity" in case of a slant line of sight. We thus prefer to directly convert the count rate into emitted power units that only requires to sum the counts overs the pixels considered. The conversion factors for the ACS camera with the 125LP filter calculated by Gustin et al. (2012) have been applied for this study, assuming a FUV color ratio of 2.5, a typical value observed for the main emission.

We estimate the power emitted into the H_2 Lyman and Werner bands on the unprojected images over well-separated regions along the main oval. These regions are indicated by the yellow ellipses on the polar projections in Fig. 1. The values of the power and local surface magnetic field derived from the VIPAL model are listed in Table 2. Fig. 5 illustrates the System III longitude dependence of the B-field intensity along the trajectory of the observed Io footprint oval and the main emission region.

On June 11 (Fig. 1), the power in the north is 2.7 ± 0.2 GW, emitted in a region where the ionospheric magnetic field intensity is 14.6 nT. The error caused by the definition of precise boundary of

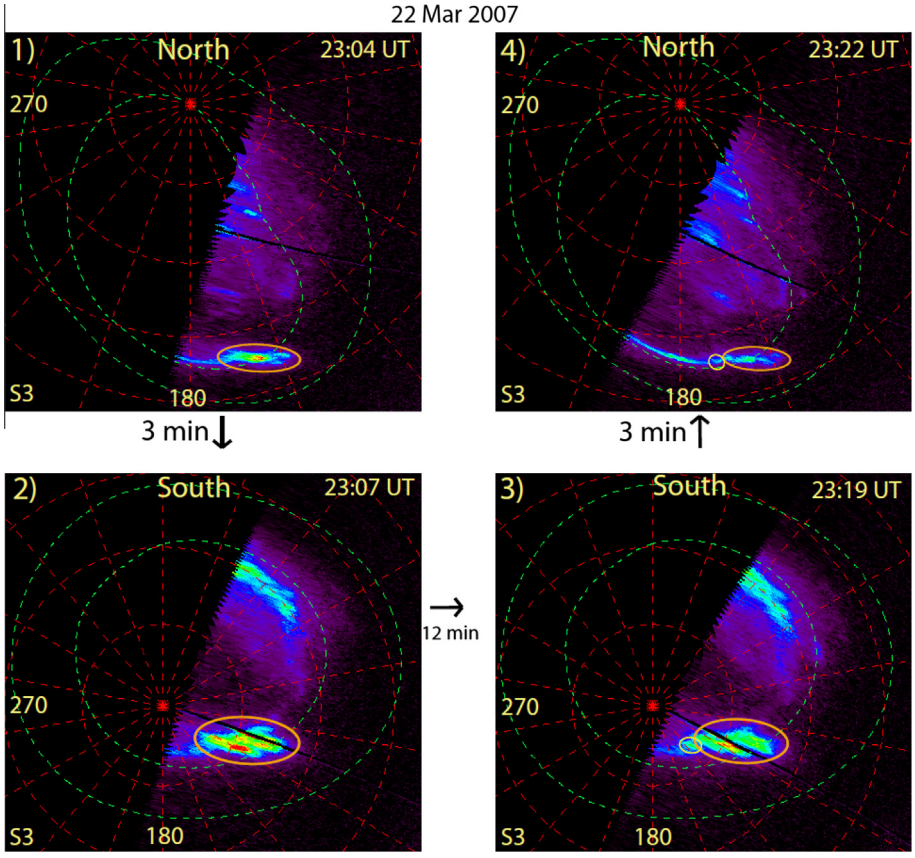

Fig. 4. Polar projections of sequence of images shown in Fig. 3. The projections are sequentially shown in System III longitude coordinates with the 180° meridian oriented toward the bottom of the page. The dark line feature crossing the images is caused by a bad anode in the ACS/SBC MAMA detector. The sequence of the exposures and their time separations are indicated. Three minutes only separate exposures (1) and (2) and (3) and (4). The red ellipses correspond to the region of the "blob" emission, while the yellow ellipses in panels (3) and (4) show the main oval segment.

the auroral region considered is obtained by moving the region of power integration by ~2 pixels in all directions corresponding to the uncertainty in the position of the boundary of the auroral feature. It is combined with the Poisson error associated with the total number of counts measured on the detector within the feature boundary. The error associated with the background subtraction is small in comparison with the other two sources. We note that a "blind" determination of a given magnetically conjugate point from one hemisphere to the other with the VIPAL model (Hess et al., 2011) leads to localization errors on the order of 2–3° of great circle. We have therefore manually corrected the selected location based on visual inspection of the conjugate features. In the south, the power is 1.8 ± 0.2 GW, with a magnetic field of 10.6 G. Similarly, the emitted power in the segment of a localized enhanced structure (orange ellipse) is 0.3 ± 0.02 GW in the north and 0.7 ± 0.02 GW in the south, with corresponding *B*-field intensity of 14.3 and 10.9 G respectively. Finally, as it is fully visible over its entire extension in both hemispheres, we integrate the total power emitted in the secondary oval (region defined by the green boundaries). We find values of 1.6 ± 0.1 GW in the north and 1.8 ± 0.1 GW in the south, leading to a marginally higher power in the south. The corresponding *B*-field intensity ranges between 10.7 and 13.7 G in the north and between 7.2 and 8.7 G in the south.

On March 22 (Fig. 4), we distinguish two regions marked by the orange and yellow ellipses. The first one indicates a particular structure close to the main emission which, as discussed above, is a possible auroral signature of magnetospheric injection. The second one corresponds to a region of main emission, whose ends are defined by the auroral signature of injection and a decrease of the main emission. The comparison of the intensity of conjugate auroral structures is summarized in Table 2. The values of the emitted power in the main emission segment are found equal to 0.7 ± 0.1 GW in the north and 0.9 ± 0.1 GW in the south. The values for the emission blob 7.8 ± 0.4 GW and 16.6 ± 0.6 GW from the couple of images 1 and 2 and 7.2 ± 0.4 and 14.0 ± 0.6 GW for images 3 and 4, leading to a north to south power ratio $P_N/P_S \sim 0.5$ for both image sets. Note that in the estimation of the emitted power, we also considered the emission hidden by the repelling wire of the ACS camera by interpolation of neighbor pixels. As mentioned before, the error bars reflect ~2 pixels uncertainty in the selection of the boundary of the auroral features combined with the Poisson error on the number of counts. In summary, the N/S power ratio is marginally less than 1 for the main oval segment, but the power of the auroral emission associated with the injection or diffuse emission is about twice larger in the south than in the north. In the next section we compare these ratios with those expected from theoretical considerations based on the assumed auroral precipitation mechanism.

Table 2
Comparison of emitted auroral power in the two hemispheres.

Figure (panel)	Feature (N/S)	Emitted power (GW)	Magnetic field intensity (G)
1(3)	Main oval N	2.7 ± 0.2	14.6
1(4)	Main oval S	1.8 ± 0.2	10.6
1(3)	Diffuse structure N	0.3 ± 0.1	14.3
1(4)	Diffuse structure S	0.7 ± 0.05	10.9
1(3)	Secondary oval N	1.6 ± 0.1	10.7–13.7
1(4)	Secondary oval S	1.8 ± 0.1	7.2–8.2
4(3)	Main oval S	0.9 ± 0.1	11.3
4(4)	Main oval N	0.7 ± 0.1	13.8
4(1)	Blob N	7.8 ± 0.4	13.3
4(2)	Blob S	16.6 ± 0.6	9.9
4(3)	Blob S	14.0 ± 0.6	9.9
4(4)	Blob N	7.2 ± 0.4	13.3

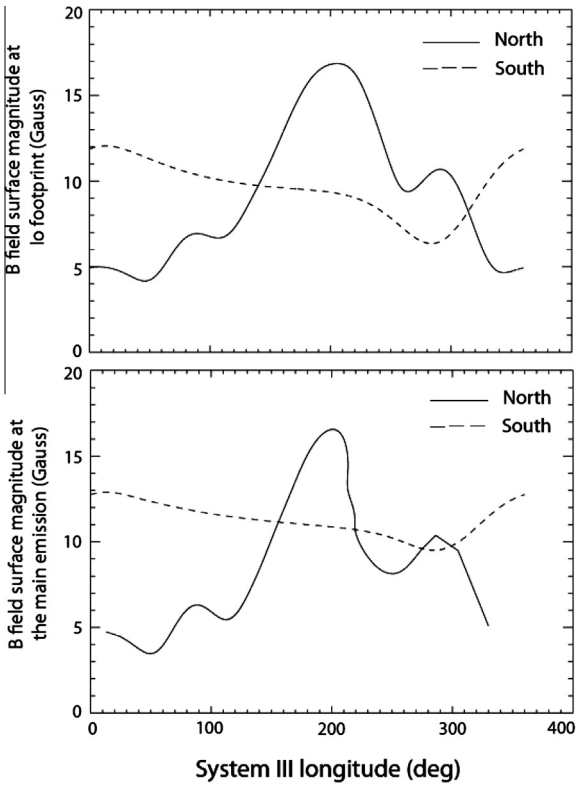

Fig. 5. Variation of the strength of the jovian magnetic field in the ionosphere as a function of the System III longitude according the VIPAL model. Top: *B*-field intensity along the locus of the Io magnetic footprint. Bottom: values along the locus of the main auroral emission.

4. Discussion

We first recall the theoretical predictions of the relative intensity of magnetically conjugate auroral emissions associated with two precipitation processes. Following the widely accepted conceptual model by Cowley et al. (2001, 2005), the jovian main auroral oval is believed to correspond to the upward leg of the large field aligned current system enforcing plasma corotation near the equatorial pane. This current closes the loop between the jovian ionosphere and the equatorial plasma sheet in the middle magnetosphere. The diffuse aurora located equatorward of the main emission is generally interpreted as a signature of electron precipitation following pitch angle diffusion into the loss cone by wave–particle interactions. In the jovian case, Mauk et al. (2002) showed that energetic particle injections are associated with transient auroral features observed equatorward of the main emission. They invoked a triggering mechanism for the observed auroral emissions involving electron scattering and electric current flowing along the boundary of the injected hot plasma cloud. At Saturn, concurrent auroral and Cassini energetic electron measurements (Radioti et al., 2009a) and numerical simulations together with simultaneous UV and ENA emissions (Radioti et al., 2013) suggested that pitch angle diffusion and electron scattering by whistler-mode waves is the main driver of the UV auroral emissions associated with injections, while field aligned currents driven by the pressure gradient along the boundaries of the cloud might have a smaller contribution.

In the case of the equinoctial observations of Saturn's FUV aurora, Nichols et al. (2009) argued that the larger emitted power in the north where the magnetic field is stronger indicates that the field-aligned currents are responsible for this emission.

For an unaccelerated hot plasma population with a near-isotropic velocity distribution, the particle energy flux is constant along a given flux tube. Consequently, the total auroral power in this case is inversely proportional to the intensity of the magnetic field line in the ionosphere. However, anisotropic velocity distributions and weak particle diffusion would both further reduce the auroral power when the ionospheric field strength increases (Stenbaek-Nielsen et al. (1973)).

By contrast, for identical Pedersen conductivities in the two hemispheres, the total field-aligned currents are also equal and the total emitted UV power is proportional to the ionospheric field strength. This conclusion was found consistent with Saturn's equinoctial results that both the difference in the ionospheric magnetic field strength at 15° co-latitude and the mean difference in the total UV power are close to 17%, in close agreement with Cowley et al. (2004) who predicted a difference of ~20%. Their calculation was based on a combination of Cowley et al.'s (2004) model of the magnetosphere–ionosphere coupling at Saturn and Knight's (1973) kinetic theory. The result was that the auroral power associated with an axisymmetric upward field-aligned current is given by:

$$P_{UV} = 0.3\frac{E_{f_o}}{j_{\|i_0}^2}\frac{\Phi_i^2}{\Delta\Phi_i}(\Delta\varpi)^2 B_i \Sigma_p^2,$$

where $j_{\|i_0}$ is the maximum FAC density which can be carried by the precipitating plasma alone, E_{f_o} the maximum energy of the unaccelerated electrons, Φ_i the magnetic flux threading the ionospheric region enclosed by the auroral annulus, $\Delta\Phi_i$ the magnetic flux contained within the auroral shell, $\Delta\varpi$ the difference in angular velocity between the plasma at the equatorward and poleward boundaries of the annulus, Σ_p is the effective height-integrated Pedersen conductivity, and B_i is the ionospheric magnetic field strength. The emitted power is then proportional to the product of strength of the magnetic field by the square of the Pedersen conductivity, assuming a common source population. In the more general case for arbitrary geometry, the UV power is proportional to the total current squared multiplied by the ionospheric field strength (Nichols et al., 2009).

We note however that the Pedersen conductivity itself varies as the inverse of the magnetic field intensity so that the auroral power then varies as $1/B_i$, similar to the diffuse aurora. Finally, the UV power depends on the total current going up the field lines, which is controlled by the ionospheric Pedersen current flowing equatorward into the layer where the angular velocity increases, which is determined by the conductivity just outside and not within the precipitation (Cowley et al., 2005). In this case, diffuse and discrete aurorae are both expected to vary proportionally to $1/B_i$ if the intensity of the surface magnetic field is the critical factor controlling the asymmetry factor.

Table 2 lists the observed emitted power in magnetically conjugate auroral features marked by yellow ellipses in Figs. 1 and 4. Comparing the two images of June 11 (Fig. 1), we derive a N/S power ratio P_N/P_S of 1.5 for the conjugate segments of the main oval, quite close to the magnetic field ratio $B_{i,N}/B_{i,S} = 1.4$. For the outer localized emission, the N/S power ratio is 0.4, while the field intensity ratio $B_N/B_S = 1.3$. The secondary ovals emit roughly equal power within the estimated error while $B_N/B_S = \sim 1.6$.

In the quasi-simultaneous observations of March 22 (Fig. 4), the corresponding segments of the main oval give $P_N/P_S = 0.8$ to be compared with the field ratio $B_{i,N}/B_{i,S} = 1.2$. The two sets of N/S ratios for the plasma injection equatorward of the main oval give $P_N/P_S = 0.47$ and 0.51, which indicates that the emitted power was nearly constant during the 18 min separating images (1) and (4) of Fig. 3. The field intensity ratio in this region is $B_{i,N}/B_{i,S} = 1.35$. We conclude, based on the limited available sample, that the conjugate power in the main oval segments we selected or in the plasma injection is neither proportional to B nor to $1/B$.

Synthetizing Table 2, we conclude that (i) different types of auroral features such as the main emission and the localized injections show a different dependence versus the surface field intensity. Opposite results are obtained for the main oval segments. Instead, the localized structure possibly corresponding to plasma injections are clearly stronger in the south in a region of magnetic field weaker than the conjugate region. They possibly involve different acceleration processes with different dependence on the local magnetic field and (ii) the precipitation along the main oval does not strictly follows a proportionality to B_i, suggesting that other processes acting along the field lines complicate the simple picture of field aligned acceleration and modify the apparent dependence on the B-field strength. One possible source would be an asymmetry in the electron density in the region of the Pedersen current flow. Similarly, the power emitted in the injected blob or in the secondary oval does not vary according to a simple $1/B_i$ law.

5. Summary

We have compared, for the first time, ultraviolet images of aurora in the two jovian hemispheres obtained close in time. This comparison indicates that the morphology shows a great deal of magnetic conjugacy when the azimuthal component of the jovian magnetic field lines is taken into account. In addition to the main emission, other features such as signatures of plasma injection and secondary oval are observed in both hemispheres. Some of the departures from conjugacy are probably caused by temporal variations occurring during the 56 min separating the north and the south exposures as it has been pointed out for the discontinuity region of the main emission, a region fixed in local time. The power emitted by the conjugate Io footprints are clearly asymmetric, with the south one brighter than the north, as it was observed on a statistical basis. The power associated with conjugate regions of the main oval or auroral signature of plasma injection observed quasi-simultaneously is generally not equal in the two hemispheres. The precipitated energy is not directly nor inversely proportional to the strength of the B-field as one would expect for diffuse precipitation or field-aligned acceleration with equal ionospheric electron density in both hemispheres. However, our limited sample suggests that the power of the outer diffuse structures decreases with the value of the surface magnetic field while the two measurements of the main oval emission remain somewhat inconclusive. The emitted power of the secondary oval is comparable in the two hemispheres while the ionospheric B field magnitude is 1.6 times stronger in the north. The power is thus neither proportional to B nor $1/B$ as would be expected for a second layer of field aligned current or for a pitch angle scattering process, respectively. These results suggest that additional factors than the value of the ionospheric magnetic field also control the asymmetry in the amount of energy precipitated in the two hemispheres. Finally, we also show that some polar emissions may be present in only one (northern) hemisphere. This lack of symmetry suggests that they are located on open magnetic field lines. This asymmetry could be a signature of reconnection with an interplanetary magnetic field dominated by its B_y component. Additional observations of the two hemispheres close in time would be very valuable to further assess possible departures from magnetic conjugacy and further investigate the north–south asymmetries in precipitated power.

Acknowledgments

This work is based on observations with the NASA/ESA Hubble Space Telescope obtained at the Space Telescope Science Institute (STScI), which is operated by AURA, Inc. for NASA under Contract NAS5-26555. A.R. and B.B. are supported by the Belgian Fund for Scientific Research (FNRS). This research was funded by the PRODEX Program managed by the European Space Agency in collaboration with the Belgian Federal Science Policy Office. Work at BU was supported by NASA Grants HST-GO-10862.01 and HST-GO-11649.01 from STScI to BU. We thank S.W.H. Cowley for useful discussions and the two reviewers for useful their suggestions.

References

Ballester, G.E. et al., 1996. Time-resolved observations of Jupiter's far-ultraviolet aurora. Science 274, 409–413.

Benkevich, L., Lyatsky, W., Cogger, L.L., 2000. Field-aligned currents between conjugate hemispheres. J. Geophys. Res. 105, 27727–27738.

Bonfond, B. et al., 2009. The Io UV footprint: Location, inter-spot distances and tail vertical extent. J. Geophys. Res. 114, A07224. http://dx.doi.org/10.1029/2009JA014312.

Bonfond, B., Vogt, M.F., Gérard, J.-C., Grodent, D., Radioti, A., Coumans, V., 2011. Quasi-periodic polar flares at Jupiter: A signature of pulsed dayside reconnections? Geophys. Res. Lett. 38, L02104. http://dx.doi.org/10.1029/2010GL045981.

Bonfond, B. et al., 2012. Auroral evidence of Io's control over the magnetosphere of Jupiter. Geophys. Res. Lett. 39, L01105. http://dx.doi.org/10.1029/2011GL050253.

Bonfond, B. et al., in press. Evolution of the Io footprint brightness I: Far-UV observations. Planet. Space Sci. http://dx.doi.org/10.1016/j.pss.2013.05.023.

Clarke, J.T. et al., 1996. Far-ultraviolet imaging of Jupiter's aurora and the Io footprint. Science 274, 404–409.

Clarke, J.T. et al., 2002. Ultraviolet emissions from the magnetic footprints of Io, Ganymede and Europa on Jupiter. Nature 415, 997–1000.

Clarke, J.T. et al., 2004. Jupiter's aurora. In: Bagenal, F., Downling, T., McKinnon, W. (Eds.), Jupiter. The Planet, Satellites and Magnetosphere. Cambridge University Press, pp. 639–670.

Clarke, J.T. et al., 2009. Response of Jupiter's and Saturn's auroral activity to the solar wind. J. Geophys. Res. 114, A05210. http://dx.doi.org/10.1029/2008JA013694.

Cowley, S.W.H., Bunce, E.J., Nichols, J.D., 2001. Origin of the main auroral oval in Jupiter's coupled magnetosphere–ionosphere system. Planet. Space Sci. 49, 1067–1088.

Cowley, S.W.H., Bunce, E.J., O'Rourke, J.M., 2004. A simple quantitative model of plasma flows and currents in Saturn's polar ionosphere. J. Geophys. Res. 109, A05212. http://dx.doi.org/10.1029/2003JA010375.

Cowley, S.W.H. et al., 2005. A simple axisymmetric model of magnetosphere–ionosphere coupling currents in Jupiter's polar ionosphere. J. Geophys. Res. 110, A11209. http://dx.doi.org/10.1029/2005JA011237.

Fillingim, M.O., Parks, G.K., Frey, H.U., Immel, T.J., Mende, S.B., 2005. Hemispheric asymmetry of the afternoon electron aurora. Geophys. Res. Lett. 32, L03113. http://dx.doi.org/10.1029/2004GL021635.

Gérard, J.-C., Gustin, J., Grodent, D., Clarke, J.T., Grard, A., 2003. Spectral observations of transient features in the FUV jovian polar aurora. J. Geophys. Res. 108, 1319. http://dx.doi.org/10.1029/2003JA009901.

Gérard, J.-C., Saglam, A., Grodent, D., Clarke, J.T., 2006. Morphology of the ultraviolet Io footprint emission and its control by Io's location. J. Geophys. Res. 111, A04202. http://dx.doi.org/10.1029/2005JA011327.

Gonzaga, S. et al., 2013. ACS data handbook, version 7.0. STScI, Baltimore. http://www.stsci.edu/hst/acs/documents/handbooks/currentDHB/acs_dhb.pdf.

Grodent, D., Clarke, J.T., Kim, J., Waite Jr., J.H., Cowley, S.W.H., 2003a. Jupiter's main auroral oval observed with HST-STIS. J. Geophys. Res. 108 (A11), 1389. http://dx.doi.org/10.1029/2003JA009921.

Grodent, D., Clarke, J.T., Waite Jr., J.H., Cowley, S.W.H., Gérard, J.-C., Kim, J., 2003b. Jupiter's polar auroral emissions. J. Geophys. Res. 108, 1366. http://dx.doi.org/10.1029/2003JA010017.

Grodent, D. et al., 2008. Auroral evidence of a localized magnetic anomaly in Jupiter's northern hemisphere. J. Geophys. Res. 113, A09201. http://dx.doi.org/10.1029/2008JA013185.

Grodent, D. et al., 2009. Auroral footprint of Ganymede. J. Geophys. Res. 114, A07212. http://dx.doi.org/10.1029/2009JA014289.

Gustin, J., Bonfond, B., Grodent, D., Gérard, J.-C., 2012. Conversion from HST ACS and STIS auroral counts into brightness, precipitated power, and radiated power for H_2 giant planets. J. Geophys. Res. 117, A07316. http://dx.doi.org/10.1029/2012JA017607.

Hess, S.L.G., Bonfond, B., Zarka, P., Grodent, D., 2011. Model of the jovian magnetic field topology constrained by the Io auroral emissions. J. Geophys. Res. 116, A05217. http://dx.doi.org/10.1029/2010JA016262.

Hess, S.L.G. et al., in press. Evolution of the Io footprint brightness II: Modeling. Planet. Space. Sci. http://dx.doi.org/10.1016/j.pss.2013.08.005.

Knight, S., 1973. Parallel electric fields. Planet. Space Sci. 21, 741–750.

Laundal, K.M., Østgaard, N., 2009. Asymmetric auroral intensities in the Earth's northern and southern hemispheres. Nature 460, 491–493. http://dx.doi.org/10.1038/nature08154.

Magain, P. et al., 2007. A deconvolution-based algorithm for crowded field photometry with unknown point spread function. Astron. Astrophys. 461, 373–379. http://dx.doi.org/10.1051/0004-6361:20042505.

Mauk, B.H., Clarke, J.T., Grodent, D., Waite Jr., J.H., Paranicas, C.P., Williams, D.J., 2002. Transient aurora on Jupiter from injections of magnetospheric electrons. Nature 415, 1003–1005. http://dx.doi.org/10.1038/4151003.

Meredith, C.J., Cowley, S.W.H., Hansen, S.W.H., Nichols, J.D., Yeoman, T.K., 2013. Simultaneous conjugate observations of small-scale structures in Saturn's dayside ultraviolet auroras: Implications for physical origins. J. Geophys. Res. 118, 2244–2266. http://dx.doi.org/10.1002/jgra.50270.

Newell, P.T., Meng, C.-I., Lyons, K.M., 1996. Discrete aurorae are suppressed in sunlight. Nature 381, 766–767. http://dx.doi.org/10.1038/381766a0.

Nichols, J.D. et al., 2009. Saturn's equinoctial auroras. Geophys. Res. Lett., L24102. http://dx.doi.org/10.1029/2009GL041491.

Østgaard, N. et al., 2005. Observations and model predictions of substorm auroral asymmetries in the conjugate hemispheres. Geophys. Res. Lett. 32, L05111. http://dx.doi.org/10.1029/2004GL022166.

Østgaard, N., Mende, S.B., Frey, H.U., Sigwarth, J.B., Åsnes, A., Weygand, J.M., 2007. Auroral conjugacy studies based on global imaging. J. Atmos. Sol. Terr. Phys. 69, 249–255.

Radioti, A., Gérard, J.-C., Grodent, D., Bonfond, B., Krupp, N., Woch, J., 2008. Discontinuity in Jupiter's main auroral oval. J. Geophys. Res. 113, A01215. http://dx.doi.org/10.1029/2007JA012610.

Radioti, A. et al., 2009a. Transient auroral features at Saturn: Signatures of energetic particle injections in the magnetosphere. J. Geophys. Res. 114, A03210. http://dx.doi.org/10.1029/2008JA013632.

Radioti, A. et al., 2009b. Equatorward diffuse auroral emissions at Jupiter: Simultaneous HST and Galileo observations. Geophys. Res. Lett. 36, L07101. http://dx.doi.org/10.1029/2009GL037857.

Radioti, A. et al., 2013. Signatures of magnetospheric injections in Saturn's aurora. J. Geophys. Res. 118, 1922–1933. http://dx.doi.org/10.1002/jgra.50161.

Stenbaek-Nielsen, H.C., Wescott, E.M., Davis, T.N., Peterson, R.W., 1973. Auroral intensity differences at conjugate points. J. Geophys. Res. 78, 559.

Waite Jr., J.H. et al., 2001. An auroral flare at Jupiter. Nature 410, 787–789.